
# Supplementary Materials for

## Quantitative mass imaging of single molecules

Gavin Young, Nikolas Hundt, Daniel Cole, Adam Fineberg, Joanna Andrecka, Andrew Tyler, Anna Olerinyova, Ayla Ansari, Erik G. Marklund, Miranda P. Collier, Shane A. Chandler, Olga Tkachenko, Joel Allen, Max Crispin, Neil Billington, Yasuharu Takagi, James R. Sellers, Cedric Eichmann, Philipp Selenko, Lukas Frey, Roland Riek, Martin R. Galpin, Weston B. Struwe, Justin L. P. Benesch, and Philipp Kukura

correspondence to: philipp.kukura@chem.ox.ac.uk

**This PDF file includes:**



**Other Supplementary Materials for this manuscript includes the following:**

**Materials and Methods**

Protein volume and refractive index calculation

All protein sequences from *Escherichia coli*, *Yersinia pestis*, *Haloferax volcanii*, *Methanocadococcus jannaschii*, *Homo sapiens*, and *Arabidopsis thaliana* genomes were downloaded from NCBI (https://www.ncbi.nlm.nih.gov/genome/) in FASTA format. The refractive index of each protein was calculated as

$$n = \sqrt{\frac{\left(\frac{2MR}{VN} + 1\right)}{\left(1 - \frac{R}{V}\right)}}$$

where $M = M_w + \sum_i (M_i - M_w)$ is the molar mass of the protein, determined from the sequence, and where the $M_W$–terms represent the loss of one water molecule per peptide bond; $R = \sum_i n_i$, is the sum of contributions from individual amino acid residues(*31*); $V = \sum_i V_i$, the specific volume, also determined from the contribution of individual residues (*32*); and $N$ is the number of residues. $M_i$, $n_i$, and $V_i$ were determined from the residue type (Table S1). Wherever ambiguous FASTA codes were encountered (B, J, X, and Z), parameters ($M_i$, $n_i$, and $V_i$) were set to the arithmetic average for the possible residue types (e.g., the average of D and N for FASTA code B).

Microscope coverslip cleaning procedure

We cleaned borosilicate microscope coverslips (No. 1.5, 24 × 50 mm, VWR, and No. 1.5, 24×24 mm, VWR) by rinsing them sequentially with $H_2O$, ethanol, $H_2O$, isopropanol, $H_2O$, ethanol and $H_2O$, followed by drying under a clean stream of nitrogen.

Landing assay procedure

Cleaned coverslips were assembled into flow chambers(*33*). Buffers were filtered through a 0.2 μm pore size syringe filter. All samples were diluted from stock solutions without further treatment. Sample proteins were diluted in 20 mM Tris-HCl, 100 mM NaCl, pH 7.4, unless otherwise stated. Typical working concentrations were 5 − 10 nM of the predominant species. After filling the flow chamber with buffer, a clean region of interest in the flow chamber was selected defined as being devoid of large scatterers on the surface, followed by flushing in 10 μl of the protein solution.

Calibration Proteins

Streptavidin (2105), bovine serum albumin (BSA, 2571), alcohol dehydrogenase (8066), β −amylase (9988), thyroglobulin (2951) and GroEL (3955) were purchased from Sigma-Aldrich. Non-muscle myosin 2B (10042) was purified as described previously(*34*), except for the addition of a halo-tag. The numbers in parentheses indicate the total number of detected particles for each calibrant from 4 − 10 separate experiments.

Myosin crosslinking

Smooth-muscle myosin (SMM) was purified as described previously (*35*) and incubated at 200 nM in ATP-containing buffer (10 mM MOPS, 150 mM NaCl, 1 mM $MgCl_2$, 0.1 mM EGTA, 0.1 mM ATP, pH 7.0) for 30 min, which induced the folded (10S) conformation. Glutaraldehyde was added to a concentration of 0.1% (v/v) and incubated for 1 min. The reaction was stopped by addition of Tris-HCl (pH 8.0) to a final concentration of 100 mM.

Electron Microscopy

Cross-linked myosin was diluted to 20 nM in buffer containing 10 mM MOPS, 150 mM NaCl, 1 mM $MgCl_2$, 0.1 mM EGTA, pH 7.0. Native myosin was diluted to 5 nM in buffer containing 10 mM MOPS, 500 mM NaCl, 1 mM $MgCl_2$, 0.1 mM EGTA, pH 7.0, which induced the extended conformation. 3 µl of sample was applied to a carbon-coated copper grid (pretreated for 45 minutes with ultraviolet light) and stained with 1% uranyl acetate. Micrographs were recorded on a JEOL 1200EX II microscope operating at room temperature. Data were collected on an AMT XR-60 CCD camera.

iSCAMS measurements of smooth-muscle myosin

Native (6S) and cross-linked (10S) myosins were diluted in buffer containing 10 mM MOPS, 500 mM NaCl, 1 mM $MgCl_2$, 0.1 mM EGTA, pH 7.0, to a concentration of 5 nM and kept on ice until use. The landing assay was performed in a flow chamber as described above.

Biotin-streptavidin binding assay

Streptavidin (Cat no. S4762) and D-biotin (Cat no. B4501) were purchased from Sigma Aldrich. Two synthetic N-terminally biotinylated peptides based on the sequences of desmoglein-3 (DSG3, biotin-EWVKFAKPCREGEDNSKRNPIAKITSDYQA) and

adrenocorticotropic hormone (ACTH, biotin-SYSMEHFRWGKPVGKKRRPVKVYPNGAEDESAEAFPLEF) were bought from Cambridge Research Biochemicals. Samples of 5 nM streptavidin and mixes of 5 nM streptavidin with 500 nM of either biotin, biotin-DSG3 peptide or biotin-ACTH peptide were prepared at the start of the day and kept on ice until use. The total number of detected particles in 4 − 9 experiments were 2105, 2167, 3131 and 936 for streptavidin, biotin-streptavidin, biotin-DSG3-streptavidin and biotin-ACTH-streptavidin, respectively.

Experimental Setup

The experimental setup is depicted schematically in Fig. S2, and is identical to that described in Fig. 4 of Cole et al.(*16*), except for the apparatus being mounted onto a 400x600x50 mm aluminium plate and enclosed to minimize the influence of external perturbations. Briefly, the collimated output of a 445 nm laser diode (Lasertack) is passed through an orthogonal pair of acousto-optic deflectors (AODs; AA Opto Electronic, DT SXY-400). A 4f telecentric lens system (Telecentric lens 1, and Telecentric lens 2) images the deflection of the beam by the AODs into the back focal plane of the microscope objective (Olympus, 1.42 NA, 60×) after passing through a polarizing beam splitter (PBS) and a quarter-wave-plate (QWP). This results in a weakly focused beam (spot size 1.5 μm) being scanned across the sample to generate the field of view. The objective collects the light reflected at the glass-water interface together with that back-scattered by the sample, which is separated from the incident light by the combination of the PBS and QWP. A second 4f telecentric system (Lens 1 and Lens 2) reimages the back focal plane of the objective, where a partially reflective mirror consisting of a 3.5 mm diameter thin layer of silver deposited onto a window selectively attenuates the reflected light by more than two orders of magnitude with respect to light from point scatterers at the surface (*16*). A final lens (Lens 3) images the sample onto a CMOS camera (Point Grey GS3-U3-23S6M-C) with 250× magnification, giving a pixel size of 23.4 nm/pixel. The focus position is stabilized with an active feedback loop using a total internally-reflected beam (not shown).

Data acquisition parameters

The camera was run close to the highest frame rate achievable for the given field of view, typically 1 kHz. Unless otherwise stated, images were pixel-binned 3x3 and time-averaged 10-fold prior to saving, giving a final pixel size of 70.2 nm and effective frame rate of 100 Hz. The power density, frame rate, exposure time and effective exposure time

after averaging were: Figs 1B-D, 2D, S3, S4A and E, S5C, S6B: 860 kW/cm$^2$, 1000 Hz, 0.95 ms, 47.5 ms; Figs 2A, 3, S4F, S5A and E, S6A and C: 420 kW/cm$^2$, 62 Hz, 1.5 ms, 300 ms; Fig S53B: 500 kW/cm$^2$, 662 Hz, 1.5 ms, 300 ms; Figs 2B and C, S5D and E: 280 kW/cm$^2$, 662 Hz, 1.5 ms, 300 ms; Figs 4A and B, S9A: 45 kW/cm$^2$, 100 Hz, 9.9 ms; Figs 4C and D, S10: 88 kW/cm$^2$, 468 Hz, 2.1 ms, 16.8 ms.

Image processing: background removal

Unless otherwise stated, analysis was performed using custom software written in LabVIEW. To remove the static scattering background from the glass surface (Fig. S3A), ratiometric images, $R$, were calculated as $R = N_{m+1}/N_m - 1$, where $N_m$ are consecutive normalized averages of several images, revealing only those features that change between the two frame batches (Fig. S3B). Each frame batch is normalized by the mean pixel value before generating the ratiometric image to avoid effects caused by slow laser intensity fluctuations. This processing is stepped through the raw movie frame-by-frame, generating a ratiometric frame stack in which a binding event appears as a (dark) point spread function (PSF), the contrast of which increases and then decreases as the midpoint of the two frame batches approaches and then moves past the time at which the protein binds (Fig. S3C,D). Unbinding events, meanwhile, appear as bright spots and are insignificant compared to binding events for landing assays on bare glass. For example, for the data shown in Fig. 1, we observed 12209 binding vs 372 unbinding events.

Image processing: particle detection and quantification

Particles were identified in the ratiometric images by an automated spot detection routine. As a first step, the convolution of the ratiometric image with the experimentally measured PSF was calculated to assist with particle detection. From the resulting image, a particle probability (PP) image was calculated as described previously(*36*), and pixels with PP > 0.3 that also corresponded to a local maximum in the convolved image were taken as candidate particles.

About each candidate pixel, an 11×11 pixel (772×772 nm) region of interest was extracted and fit to a model PSF to extract the contrast. In place of the more conventional 2D Gaussian function, we used a difference of two concentric 2D Gaussians to model the effect of the circular partial reflector in the Fourier plane on the PSF(*16*). The width and amplitude of the second Gaussian (arising from the presence of the partial reflector) were dictated by the relative sizes of the partial reflector and objective back aperture, and the reflectance of the mask, thus avoiding additional parameters in the fit:

$$f(x,y) = A\left( e^{-\left[\frac{(x-x_0)^2}{2\sigma_x^2}+\frac{(y-y_0)^2}{2\sigma_y^2}\right]} - \frac{(1-T)}{s} e^{-\left[\frac{(x-x_0)^2}{2(s\sigma_x^2)}+\frac{(y-y_0)^2}{2(s\sigma_y^2)}\right]} \right) + b$$

where $s = 8.52/3.5$, is the ratio between the diameter of the objective back aperture and the diameter of the partial reflector, and T is the transmission of the mask. The contrast reported is therefore $A\left(1 - \frac{(1-T)}{s}\right)$, corresponding to the peak value of this function as it appears in an image. If the fitted function was too eccentric it was rejected as not arising from a single molecule binding event. This was determined by taking the ratio of the smaller to the larger of the two fitted standard deviations ($\sigma_x$ and $\sigma_y$), and rejecting the fit if this ratio was below 0.7.

As described above, the sliding ratiometric analysis results in a single molecule binding event appearing in several consecutive frames, with increasing and then decreasing contrast. To avoid over-counting particles, and to extract the most accurate measure of the particle contrast, the fits were grouped into those arising from a single particle based on their spatial and temporal location in the image stack. Points lying within 1 pixel of each other, and arising from frames within a window size of twice the temporal frame averaging were classified as one particle. The contrast of a given particle as a function of time in the image stack then exhibits a linear growth up to a maximum, followed by a linear decrease. For each particle, this profile was fit to a pair of straight lines with gradients of equal magnitude but opposite sign, and the peak contrast taken to be the best estimate of the true particle contrast (Fig. S3D).

To extract accurate values for the mean contrast (Fig. 2), the resulting contrast distribution was fit to one or the sum of two Gaussian peaks (a Gaussian function when a single peak was well-isolated from other detected species, or the sum of two Gaussians where two peaks were not fully separated). Fitting was performed using the maximum-likelihood procedure as implemented in MEMLET(*37*). To optimize the fit by maximum-likelihood, it was necessary to reject outlying data points from the distribution (e.g. from the presence of some smaller species in solution, or larger aggregates). For unimodal distributions, for example, outliers were defined as those points either with a contrast less than the lower quartile minus 1.5 times the interquartile range, or greater than the upper quartile plus 1.5 times the interquartile range.

The dependence on sequence mass of the average value of the contrast determined in this way for each of the 8 proteins listed above was fit to a straight line in order to calibrate the system. We used the difference between the line of best fit and the measured data to assess the accuracy of the technique, resulting in the average deviation of 1.9% from the sequence mass reported in the main text.

Surface vs solution distributions and corrections

In landing assays, we detect individual molecules binding to the cover glass surface, rather than directly in solution. As a result, variations in surface affinities and/or collision rates could in principle affect the surface-measured distribution from the true solution distribution. We can, however, extract binding rates directly from our experimental data. For this, we employ standard flow cells(*33*), that exhibit large surface-to-volume ratios. As a result, binding to the surface reduces the analyte concentration throughout the experiment, as can be seen in Fig. 1D. We remark that this decay in sticking frequency cannot be attributed to surface saturation, because (a) we can add more sample to a flow chamber a few times and still observe binding, (b) for a 4×9 μm field of view, a tightly packed monolayer of 5 nm diameter particles would contain ~$1.8\times10^6$ particles, while we typically measure $10^3$ binding events in an experiment, and (c) the lack of unbinding implies that we deplete the concentration in solution with time. The measured drop in binding frequency is well described by an exponential decay, consistent with a simple first-order process of protein molecules in solution binding to the glass surface with a given rate constant (Fig. S4A), which provides representative decay constants from multiple movies (Fig. S4B). Because we have sufficient mass resolution to distinguish different oligomeric states, we can characterise the decay in binding rate for each oligomeric state (Fig. S4C), measuring a rate constant which is a function of the surface sticking probability and the collision rate, which in turn is proportional to the diffusion coefficient.

The values of these rate constants for different oligomers and different species studied in this manuscript exhibit variations of less than ±25% from the mean decay for all oligomeric species per protein (Fig. S4C). For BSA, Env, smooth-muscle myosin and GroEL we observe a decrease in decay rate with molecular weight. For systems where we observe decay of a native, globular oligomeric structure into smaller subunits (ADH, βamylase), the pattern is inverted. Importantly, the decay rates are highly reproducible with

narrow standard deviations, demonstrating that they can be characterised with high accuracy on an oligomer-to-oligomer basis. We found excellent correlation between the absolute rate constant and the (molecular weight)$^{-1/3}$, i.e. the scaling of the diffusion coefficient with mass assuming spherical objects, suggesting that the surface affinity for different oligomeric states, and indeed different proteins, does not vary significantly (Fig. S4D).

To probe the effect of diffusion and surface attachment on oligomeric distributions and resulting thermodynamics parameters, we can apply a correction to the counted numbers of each oligomer depending on the measured binding rate constant. Assuming that any change in the equilibrium distribution as a result of this dilution is slow compared to the timescale of the experiment, then to accurately count the proportion of each oligomer present in solution, one would have to integrate over the exponential decay in binding events from the addition of sample (time, $t$ = 0) until all binding has ceased. Experimentally, meanwhile, we effectively integrate from some time, $t_0 \approx 15$ s, after addition of sample up to a later time, $t_f$, when the acquired movie ends. We can relate these two via

$$N_i = M_i \frac{e^{k_i t_0}}{1 - e^{-k_i (t_f - t_0)}}$$

where $N_i$ is the number of particles of oligomer $i$ counted over the full integral, $M_i$ is the number measured experimentally, and $k_i$ is the binding rate constant for oligomer $i$.

As shown for BSA (Fig. S4E) corrections produce noticeable, but nevertheless small corrections to the mass distributions. One may a priori assume that the correctin should lead to an increase in the dimer fraction because of compensation for diffusion, we find the opposite to be true. This is caused by the fact that we have to take into account a delay between addition of the sample and observation of binding events, which is usually on the order of 15 s. During this time, more lower oligomers are lost to the surface, which ultimately leads to the counterintuitive correction factor. We observe similar effects for our Env-Banlec experiments (Fig. S4F), where the correction causes changes in the mole fractions that are within the error associated with our ability to model the experimental data.

We conclude that non-specific binding to microscope cover glass only weakly influences oligomeric distributions by iSCAMS, suggesting that our measurements are representative of solution distributions, especially given the fact that they can be corrected by quantifying the probability of surface attachment and diffusion coefficient as a function of oligomeric state.

Accuracy, noise floor, resolution and precision

The mass deviation between sequence mass and measured mass according to a linear correlation from calibration proteins was <5 kDa. Comparison with molecular shape factor as extracted from structural data exhibited no clear correlation in magnitudeor in sign (Fig. S6A). Therefore, at this stage we cannot quantitatively connect accuracy, mass and refractivity beyond a general rule that the accuracy is limited to a few kDa, which causes the percentage deviation to increase for smaller object mass as shown in the upper panel of Fig. 2A.

The noise floor of our approach, as defined by the standard deviation of background images recorded in the absence of biomolecules, decreases as expected for a shot noise-limited process for image averaging up to several tens of ms, after which it begins to deviate, with a minimum near 300 ms (Fig. S6B). We believe that the deviation is largely caused by sample drift, causing the surface roughness to begin to contribute to the ratiometric images. The noise floor represents the instrumental limit to mass resolution manifested in the width of the recorded mass distributions. In addition, we found that this width increases with mass (Fig. S6C), an effect that may be expected in the presence of an additional uncertainty that scales with size of the object measured. We currently believe that the source of this additional broadening is largely caused by the rough glass surface, which exhibits ±40% peak-to-peak variations in reflectivity in our experimental arrangement.

The theoretical precision, at least in the context of unimodal mass distributions is given by $\sigma/\sqrt{N}$, where $\sigma$ is the standard deviation of the distribution and $N$ the number of events measured. We find that this relationship frequently holds only for $N$<100, leading to a precision on the order of 2% of the object mass (see Fig. 2D). As above, we believe that the most likely limiting factors are the glass roughness and our ability to precisely

determine the focus position from experiment to experiment in a repeatable fashion, inducing contrast and thus mass variations beyond the theoretical expectation.

Lipid nanodiscs preparation and procedure

Membrane scaffold proteins were expressed in *E.coli*, purified and assembled by addition of lipids in the molar ratios specified in Table S2, followed by purification by size exclusion chromatography as described previously(*38*). The nanodiscs were diluted to 10 nM in 20 mM Tris, 100 mM NaCl, pH 7.4, and nonspecific binding to a glass surface was measured according to the procedure described above. For comparison with expected masses for each sample, we took literature values (Table S3) for the mass of the MSP1D1 nanodisc with DMPC (1,2-dimyristoyl-sn-glycero-3-phosphocholine), which we took as a reference, as measured by a variety of techniques to provide a range of expected masses. For each of these, including our own, we calculated an expected mass for the MSP1ΔH5 nanodisc with DMPC. This was done by subtracting the mass of the protein component and scaling the resulting mass of lipid by the reduction in area of the bilayer patch calculated from the square of the reduction in diameter of the nanodisc as measured by size exclusion chromatography (SEC), dynamic light scattering (DLS) and electron microscopy (EM). The expected mass of the nanodisc follows by addition of the MSP1ΔH5 protein mass (Tables S3 and S4).

Similarly, for the MSP1D1 nanodiscs with varying lipid composition, we calculated a range of expected masses from the various reported measurements of the reference nanodisc. We scaled the measured lipid mass according to the expected changes due to different total number of lipid molecules per nanodisc (from the protein:lipid assembly ratio) and different average mass per lipid molecule. Again, addition of the mass of protein leads to the expected masses of the nanodiscs (Tables S5 and S6). The total number of detected particles were 14216 (MSP1D1-DMPC), 3041 (MSP1D1-DMPC/PC14:1/Chol), 2292 (MSP1D1-PC14:1/Chol), 2277 (MSP1Δ1- DMPC) from 2 − 12 experiments.

Env and BanLec preparation and procedure

Env SOSIP (BG505) and BanLec were prepared as described previously(*39*), either in the presence or absence of kifunensine. The proteins were each diluted to 5 nM in phosphate buffered saline (PBS) and binding to a glass surface was imaged in a flow chamber as described for the landing assay. The total number of detected particles were

15391 and 8048 for kifunensine-treated and wildtype Env, respectively.

For the interaction studies between Env and BanLec, Env was diluted to 20 nM in PBS. BanLec was diluted to 2-fold the working concentration in PBS. The protein dilutions were kept on ice until use. Env was mixed 1:1 with either PBS (as a control) or BanLec, and incubated for 5 min at room temperature. Next, 20 µl of the mixture were flushed into a PBS-filled flow chamber, and landing on the glass surface immediately recorded. The kernel density estimates of the probability densities shown in Fig. 3A were generated using a Gaussian kernel with bandwidth of 30 kDa. The number of each observed Env cluster was determined by counting landing events within resolvable contrast intervals, i.e. monomers, dimers, trimers, tetramers and above. In order to determine how many individual Env molecules were present in each population, the number of landing events was multiplied with the respective number of Env units per oligomer (1 for monomeric Env, 2 for dimeric Env, 3 for trimeric Env, etc.). In this way, the fraction of Env molecules in clusters and relative abundance of the different species (Fig. 3B) could be calculated.

In order of increasing BanLec concentration, the total number of detected particles were: 4446, 4841, 3068, 3106, 6258, 3893, 7370, 4198, 3412, 3027, 3674, 4287, 3790.

Modelling of Env-BanLec interaction

We modeled the Env (A) BanLec (B) system as

$$A + A \rightleftharpoons A_2 \qquad K_d$$

$$A + B \rightleftharpoons AB \qquad K_{BanLec}$$

$$A_nB_n + A \rightleftharpoons A_{n+1}B_n \qquad K_{Env}$$

$$A_{n+1}B_n + B \rightleftharpoons A_{n+1}B_{n+1} \qquad K'_{BanLec}$$

From these equilibria, the concentration of each oligomer can be expressed in terms of a combination of equilibrium constants and powers of $[A]$ and $[B]$. Using the fact that the total number of each monomer is conserved, i.e.

$$[A]_0 = [A] + 2[A_2] + [AB] + \sum_{i=m}^{\infty} \sum_{n=m-1}^{m} m[A_mB_n]$$

$$[B]_0 = [B] + [AB] + \sum_{i=m}^{\infty} \sum_{n=m-1}^{m} n[A_mB_n]$$

where $[A]_0$ and $[B]_0$ are the initial concentrations, we thus obtained two simultaneous equations to solve (numerically) for $[A]$ and $[B]$ in terms of the equilibrium constants and the initial concentrations. Once $[A]$ and $[B]$ are known, the concentrations of all other species follow from the equilibrium conditions.

We obtained very good agreement with experiment for $K_{Env} \simeq 8$, $K_{BanLec} \simeq 0.4$, $K'_{BanLec} \simeq 0.12$, and $K_d \simeq 0.004$ all in units of $(nM)^{-1}$. The initial concentration of Env in the calculation was taken to be 10 nM.

SLB preparation

CultureWell silicone gaskets (Grace Bio-Labs) were cut and placed onto a freshly cleaned coverslip providing four independent 30 − 50 µl sample chambers on the same substrate. Stock solutions of 1,2-dioleoyl-sn-glycero-3-phosphocholine (DOPC) and 1,2-dioleoyl-sn-glycero-3-phospho-L-serine (DOPS) in chloroform were purchased from Avanti Polar Lipids (Alabaster, AL). The DOPC:DOPS (3:1) mixture was dried to a film, kept under vacuum for at least 1 h and brought to a concentration of 1 mg $ml^{-1}$ in bilayer buffer (10 mM HEPES, pH 6.8, 200 mM NaCl, 2 mM $CaCl_2$). Using a mini-extruder (Avanti Polar Lipids), the suspension was then forced 21 times through a single membrane with a pore size of 100 nm. SLBs were formed by vesicle fusion inside the chamber on cleaned coverslips that have been passed through a blue flame. After 5 − 10 min incubation, excess vesicles were removed from the chamber by rinsing with 10 mM sodium phosphate buffer, pH 7.0.

α-Synuclein preparation

The construct was expressed and purified as described previously(*40*), lyophilized and stored at −20 °C. The lyophilized protein was dissolved at a final concentration of 1−1.5 mM in 20 mM sodium phosphate, pH 7.0. In order to allow complete dissolution of the protein powder, the pH of the α-synuclein solution was adjusted to 7.0 with 1 M sodium hydroxide.

α-Synuclein aggregation imaging and analysis

Before addition to the SLBs, the protein was diluted in sodium phosphate buffer, and 10 µl of α -synuclein solution added to a sample volume of 30 µl, yielding the final reported concentrations. Addition of α-synuclein was recorded at 100 frames/s and aggregate

formation was followed for 20 s. The acquired images consisted of 512×512 pixels with a pixel size of 23.4 nm/pixel, resulting in a field of view of 12×12 μm. As with the protein binding assays, these images were 3×3 pixel-binned before additional processing, giving a final pixel size of 70.2 nm/pixel. To capture the initial growth, the entire image stack was divided by a background image. The background was chosen as the average of frames before addition of α-synuclein, which can be observed as a brief disturbance during Movie S2. After selecting an 11×11 pixel region of interest centred on each growing aggregate, we fitted this region in each frame to the difference-of-two-Gaussians model function, as described for the analysis of protein landing events. The contrast was plotted as a function of time, and the initial growth rate was determined by a linear fit for 0.1 − 1 s of data after addition of α -synuclein, depending on concentration.

Preparation of biotin-PEG flow chambers for actin polymerization assays

Microscope cover glass (No. 1.5, 24×50 mm, VWR) was sonicated sequentially in 2% Hellmanex, $H_2O$ and ethanol each for 10 min, then 0.1 M KOH for 15 min and finally 5 min in $H_2O$. In between each step, they were washed with $H_2O$ to remove excess solution from the previous step. All coverslips were individually rinsed with $H_2O$ and ethanol, then blow-dried with a clean stream of nitrogen. A solution of 2 mg $ml^{-1}$ mPEG-silane (MW 2000, LaysanBio) and 0.1 mg $ml^{-1}$ biotin-PEG-silane (MW 3400, LaysanBio) in 80% ethanol at pH 2.0 (adjusted with HCl) was prepared immediately before being sandwiched between two cleaned coverslips. The sandwiches were incubated in petri-dishes at 70 °C for 16 h. The biotinylated coverslips were vigorously rinsed with $H_2O$ and ethanol in an alternating fashion removing any dried excess PEG, then blow-dried with a clean stream of nitrogen. Small coverslips (No. 1.5, 24 × 24 mm, VWR) were rinsed with $H_2O$ and ethanol in an alternating fashion and blow-dried with nitrogen. Flow chambers were assembled as described above. The flow chambers were stored in a dry nitrogen atmosphere at −20 °C.

Actin *in vitro* polymerization

Rabbit skeletal muscle actin was purified as described previously(*41*). Biotinylated actin was purchased from Cytoskeleton Inc. (Denver, USA, Cat. no. AB07-A). Biotin (Cat. no. B4501) and avidin (Cat. no. A9275) were purchased from Sigma Aldrich. A biotin-PEG flow chamber was filled with G-actin buffer (2 mM Tris-HCl, 0.2 mM $CaCl_2$, pH 8.0),

flushed with 40 µl of 10 µg ml$^{-1}$ avidin in G-actin buffer and incubated for 5 min. Excess avidin was flushed out with 40 µl of G-actin buffer. Immediately before addition to the flow chamber, polymerization of a mixture of G-actin and 1% biotinylated G-actin (final concentrations: 300 − 1000 nM actin, 3 − 10 nM biotin-actin) in G-actin buffer containing 0.2 mM ATP and 2 mM DTT was induced by adding 1/10 of a volume of 10× KMEH buffer (1× concentration: 10 mM HEPES, 50 mM KCl, 2 mM $MgCl_2$, 1 mM EGTA, pH 7.4). A volume of 50 µl of the polymerization mixture was flowed into the chamber. A 9 × 9 µm$^2$ field of view was recorded at 468 frames/s.

Actin polymerization data analysis procedure

The movies of actin polymerization were analyzed using custom software written in LabVIEW. The raw video was 2×2 pixel-binned resulting in an effective pixel size of 46.8 nm/pixel. To visualize the actin filaments on top of the signal from the glass surface roughness, a background image was created by taking a median of 20 raw images, and used to background-correct subsequent frames. To reduce shot noise, 8 consecutive frames were averaged, which gave an effective frame rate of 58.5 Hz. Actin filament tips were tracked by selecting a region of interest that included only the tip to be analyzed. Each frame of this region was then fit using a filament tip model function(*42*), consisting of a Gaussian wall $w(x, y)$ starting at $x_0$ and $y_0$ running in direction θ with width σ:

$$w(x,y) = exp\left[-\frac{\big((x-x_0)\sin\theta + (y-y_0)\cos\theta\big)^2}{2\sigma^2}\right]$$

which is attached to half of a symmetric 2D Gaussian $g(x, y)$ having its centre at $x_0$ and $y_0$ with width $\sigma$

$$g(x,y) = exp\left[-\frac{(x-x_0)^2 + (y-y_0)^2}{2\sigma^2}\right]$$

The two functions are attached to each other by defining the border $b(x, y)$ between them in the following manner:

$$f(x,y) = (y-y_0)\cos\left(\theta - \frac{\pi}{2}\right) - (x-x_0)\sin\left(\theta - \frac{\pi}{2}\right) + 0.5$$

$$b(x,y) = \begin{cases} 0, f(x,y) < 0 \\ f(x,y), 0 \le f(x,y) \le 1 \\ 1, f(x,y) > 1 \end{cases}$$

The tip function $t(x,y)$ with an amplitude $A$ is then created as:

$$t(x,y) = A\big[b(x,y)g(x,y) + \big(1 - b(x,y)\big)w(x,y)\big]$$

A LabVIEW representation of this function fitted the filament tip images using the Levenberg-Marquardt algorithm. The filament tip position was defined by the best fit values for $x_0$ and $y_0$. The growth axis of the trajectory was aligned with the $x$-axis of the coordinate system by a respective rotation. Step traces as shown in Fig. 4D were created by plotting the $x$-axis position *vs.* time.

Steps were automatically detected by a LabVIEW implementation of a previously described step finding algorithm (*43*). Briefly, we describe the step traces as a sequence of values, $x_1, x_2, \ldots, x_n$, which are drawn from an unknown number of normal distributions of equal variance ($\sigma^2$) but different means ($\mu$). The algorithm then searches for the change points of $\mu$, i.e. step positions, in the data series, one at a time. This is done by segmenting the sequence at each position $k = 1, \ldots, n-1$ and testing the null hypothesis

$$H_0: \mu_1 = \mu_2 = \cdots = \mu_n$$

against the alternative

$$H_1: \mu_1 = \cdots = \mu_{k_0} \neq \mu_{k_0+1} = \cdots = \mu_n$$

where $1 < k_0 < n$ is the unknown position of a change point. Once a change point is found the sequence is divided into two sequences before and after the accepted change point. For each sequence the process is repeated until no more change points are found, i.e. the null hypothesis is accepted. Hypothesis testing was performed based on the principle of minimization of the Schwarz information criterion (*SIC*), defined by

$$SIC = p\log n - 2\log L(\theta)$$

where $L(\theta)$ is the maximum likelihood function for the model, $p$ is the number of free parameters in the model, and $n$ is the sample size. With $SIC(n)$ being the *SIC* under $H_0$, and $SIC(k)$ being the *SIC* under $H_1$, for a change point at a position $k = 2, \ldots, n-2$. The hypothesis $H_0$ is accepted if $SIC(n) \leq \min_k SIC(k)$, otherwise $H_0$ is rejected if there is a $k$ for which $SIC(n) > SIC(k)$. The change point position is chosen to be where $SIC(k)$ is smallest in the data sequence. For our case, assuming a shifting mean and a constant variance, the two SIC values are obtained as

$$SIC(n) = n\log 2\pi + n\log \sigma^2 + n + 2\log n$$

$$SIC(k) = n\log 2\pi + k\log \sigma_1^2 + (n-k)\log \sigma_n^2 + n + 3\log n$$

where $\sigma^2 = \frac{1}{n}\sum_{i=1}^{n}(x_i - \bar{x})^2$, $\sigma_1^2 = \frac{1}{k}\sum_{i=1}^{k}(x_i - \bar{x})^2$, and $\sigma_n^2 = \frac{1}{n-k}\sum_{i=k+1}^{n}(x_i - \bar{x})^2$. Since this method works solely based on comparison of the *SIC* values, it does not require any input other than the data sequence and finds steps without user bias. We only included change points that are at least three data points apart from another, in order to eliminate steps that are found based on large fluctuations on a very short timescale. We emphasize that changing the minimum delay had a negligible effect on the obtained step sizes (Fig. S10E,F). The distribution of step sizes was described by a Gaussian mixture model using the expectation maximization algorithm in MatLab. Errors of the fitting parameters were estimated using a bootstrap procedure with 1000 bootstrap samples.

Phalloidin-actin control experiment

We attempted a control experiment with static actin filaments to provide a baseline in terms of filament end tracking and to determine whether any end displacements could result from the entire filament moving across the surface. Unfortunately for this experiment, actin filaments are generally dynamic at their ends and the absence of G-actin in solution causes their depolymerisation. G-actin at the critical concentration causes no net growth, but subunits will exchange at the filament tips. To minimize this effect, we used the actin filament stabilizer phalloidin. A mixture of 10 μM G-actin and 0.1 μM biotin-G-actin in G-actin buffer containing 0.2 mM ATP and 2 mM DTT was polymerized for 1 h by adding 1/10 of the volume of 10× KMEH. It was then diluted 5-fold in 1× KMEH and mixed with 3 μM phalloidin (Sigma P2141) in 1× KMEH. The filaments and phalloidin were incubated overnight at 4 °C. On the day of the experiment the phalloidin-stabilized filaments were diluted to 100 nM in 1× KMEH and kept on ice until use. The biotin-avidin-flow chambers were prepared as described above, then 30 μl phalloidin-actin were added. The attachment of filaments was monitored under similar imaging conditions as the polymerization experiments.

The presence of phalloidin markedly reduced any dynamics at the filament tips, but did not fully stop them at our levels of sensitivity. We could, however, correlate the displacements of the two ends of individual filaments in order to rule out that any tip

position fluctuations are caused by an overall movement of the filaments. We selected 9 short phalloidin-stabilized filaments whose two tips were both visible and isolated from other filaments (Fig. S10A). We tracked both tips and determined their displacements along the filament axis as described above, orienting the resulting trajectories such that the two tips were facing opposite directions. We found no correlation between the displacements of the two tips on the same filament (SFig. 10B) suggesting that length fluctuations at the two filament ends are not caused by movement of the filament.

Actin filament growth simulation

To test the fidelity of our step finding algorithm, custom written software in LabVIEW created a movie of growing actin tips. The model function described in actin polymerization data analysis procedure was used to generate actin filament tips with amplitude $A = -0.06$ and width $\sigma = 1.7$ pixels in a 15×15 pixel image, which is similar to the experimental values assuming a pixel size of 46.8 nm. The experimental shot noise level was determined by dividing the respective pixel values of one frame in the experimental videos (averaged to 58.5 Hz) by those of the previous frame and determining the standard deviation of the pixel values in the resulting differential images. The LabVIEW Gaussian noise generator was used to produce images with the experimental shot noise level ($1.8\times10^{-3}$), which was then added to the filament tip images. The length of the actin filament tip was extended or shortened in consecutive frames by moving the tip position a defined distance (here 1, 2, 2.7, 4, 5 or 8 nm) forward or backward along the filament axis.

The dwell times of the tip between forward steps or backward steps were randomly chosen from two pools of exponentially distributed dwell times generated according to $T = -\ln U/k$, where $T$ is the dwell time, $U$ a uniformly distributed random number between 0 and 1, and $k$ the rate constant. The rate constant for subunit attachment (forward step) $k_1$ was 4.887 $s^{-1}$ and the rate for subunit detachment (backward step) $k_{-1}$ was 2.103 $s^{-1}$, both based on experimentally determined kinetics (Fig. S10C at 0.3 μM). The dwell times were used to create a sequence of attachment and detachment events, which were treated independently, for a time period of at least the length of the simulated video. For a simulated video of 15 s at 58.5 Hz frame rate the program checks each frame whether an event is due according to the sequence of events generated before and either executes the

event or leaves the filament unchanged. Multiple events happening during one frame time is possible and accounted for. The simulated image sequences are analyzed in the same way as the experimental videos as described in the actin polymerization data analysis procedure section. The simulation with 2.7 nm step size matches our step size histogram in Figure 4E well, with smaller steps detectable, albeit returning a larger than defined step size (Fig. S10D). Overall, these simulations demonstrate that the assumption-free step-detection algorithm is capable of robustly identifying and quantifying 2.7 nm given the experimental noise level.

Determination of actin macroscopic growth rates

A smoothing spline was fitted to the 2D trajectories obtained from tracking actin filament tips, as in the actin polymerization data analysis procedure section. The length of this spline was used as the average tip displacement *d*. The average elongation velocity *v* of the filament tip was calculated according to

$$v = \frac{d \times F_r}{n}$$

where $F_r$ is the frame rate and *n* the number of frames, leading to the average elongation rate

$$r = \frac{v}{A_s}$$

where $A_S$ is the actin subunit size, assumed to be 2.7 nm(*44*). This procedure was repeated for a number of actin filaments growing at different actin concentrations. The elongation rate as a function of actin concentration can be described by

$$r = k_{+1}[actin] - k_{-1}$$

where $k_{+1}$ is the subunit association rate constant, $k_{-1}$ is the subunit dissociation constant and $K_{crit} = k_{-1}/k_{+1}$ is the critical concentration for actin polymerization(*45*). The critical concentration (129 ± 151 nM) and rate constants ($k_{+1}$ = 16.3 ± 5.0 $\mu M^{-1}$ $s^{-1}$ and $k_{-1}$ = 2.1 ± 2.4 $s^{-1}$) obtained from Figure S10C agrees well with previous studies(*46*).

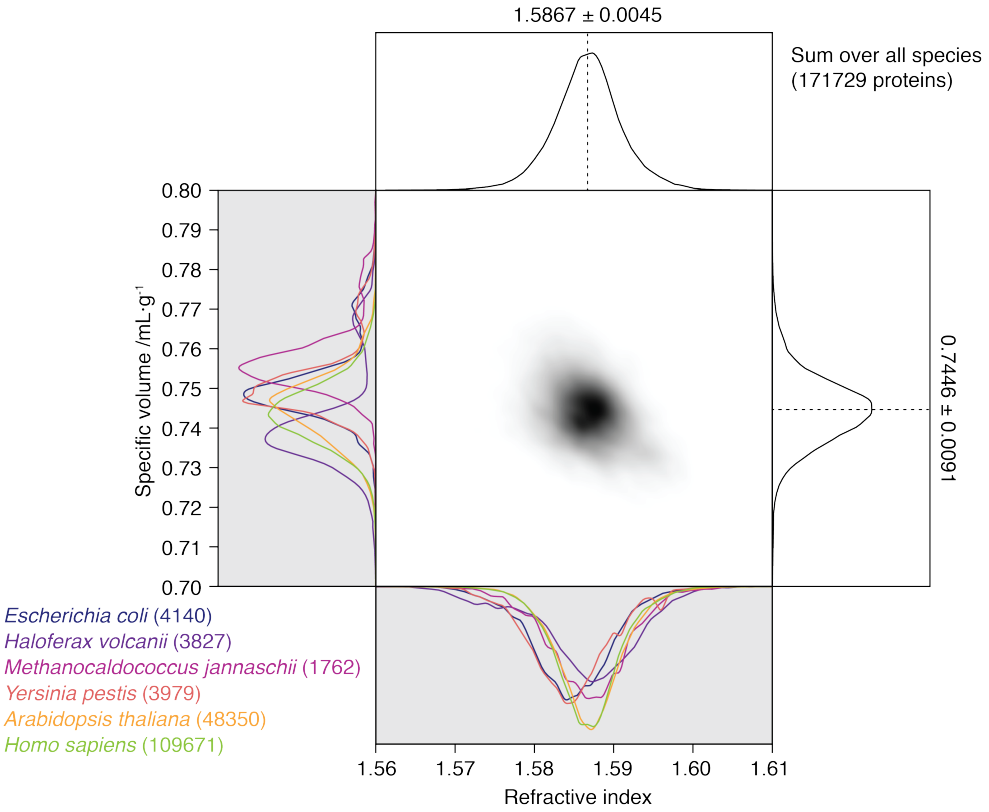


**Fig. S1.**

One-dimensional distributions of refractive index (top, bottom) and specific volume (left, right) for all proteins in six genomes, as calculated from the amino acid sequences, and the two-dimensional distribution of both quantities (middle). The top, right, and middle panels show the combined data from all genomes. The left and bottom panels show the respective distributions for the separate genomes, renormalized to have identical areas.

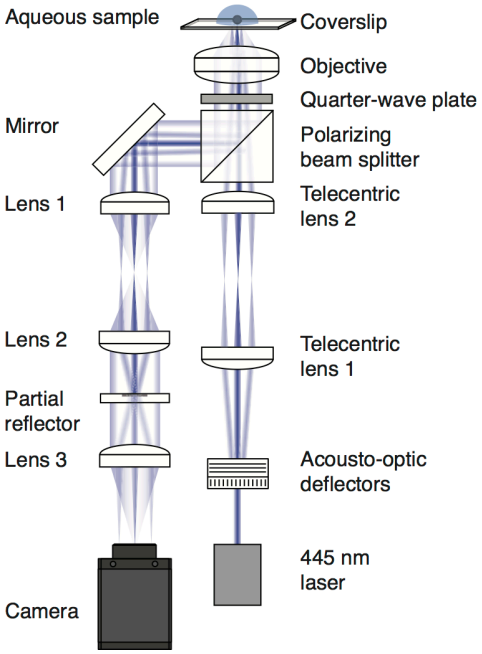


**Fig. S2.**

Schematic of the experimental setup.

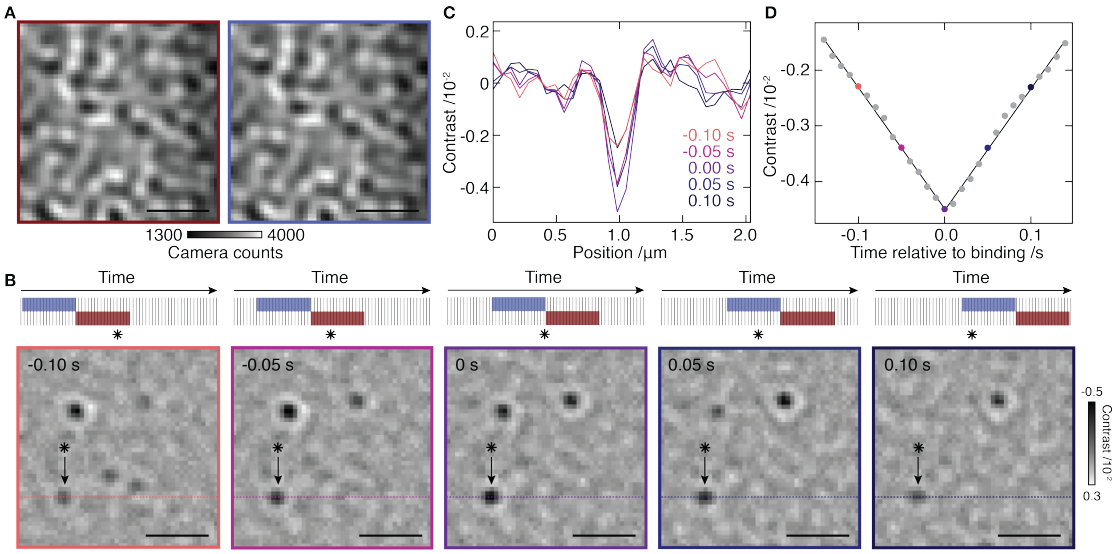


**Fig. S3**

**Data analysis.** (**A**) Raw camera images before and after the landing event in **B-D** showing image contrast due to coverslip roughness. (**B**) Illustration of the image averaging and differential imaging approach. The asterisk marks a landing event. Individual images are averaged into two consecutive blocks (blue and red), which are normalized and divided to provide differential contrast. The mid-point is scanned in time, meaning that the signal from stochastic landing events grows and fades, as indicated by the black arrow. Scale bars: 1 µm. (**C**) Corresponding cross-sections for the particle highlighted in **B**. (**D**) Corresponding signal magnitudes extracted by a fit to the PSF and fit (black).

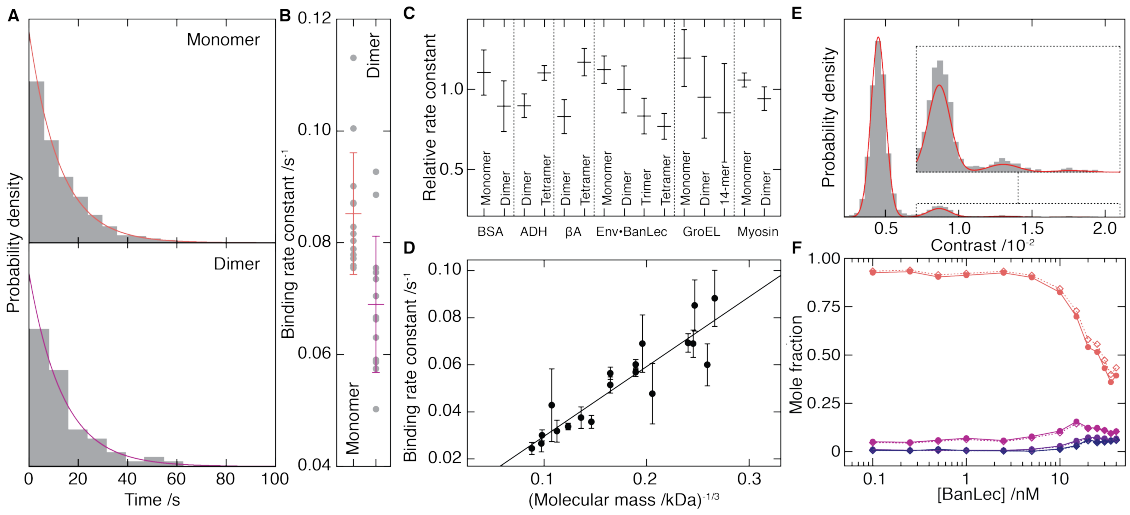


**Fig. S4.**

**Solution vs surface mass distributions.** (**A**) Changes in binding time distributions for BSA monomers and dimers from the same data as shown in Fig. 1 and corresponding exponential fits. (**B**) Resulting binding rate constants for 11 different movies. (**C**) Binding constants for a variety of proteins exhibiting more than one oligomeric state studied in this work, normalized to the average binding constant for each protein. (**D**) Plot of binding constant vs (molecular weight)$^{-1/3}$, except for those exhibiting inverted behavior but including protein samples exhibiting only a single oligomeric state as well as those in **C**, together with a linear fit describing the behavior expected from diffusion scaling. (**E**) BSA mass distribution before (solid bars) and after (red line) scaling for mass-dependent diffusion. (**F**) Env-BanLec oligomeric evolution before (solid) and after (dashed) correction for surface effects.

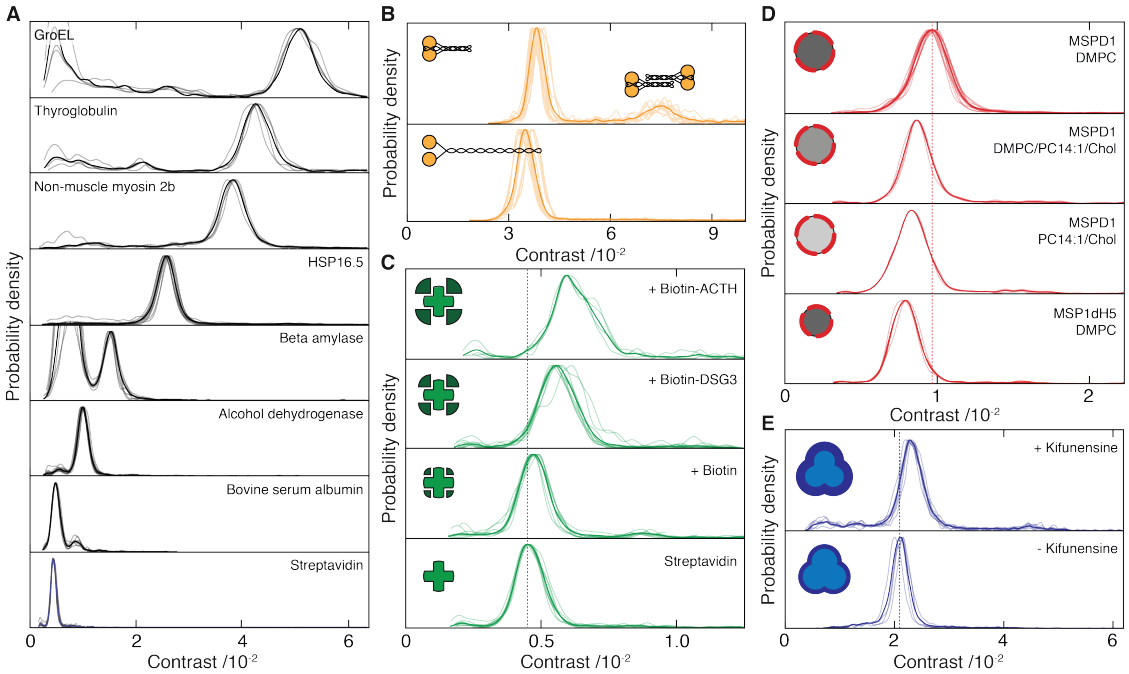


**Fig. S5**

Kernel densities for Fig.2 in the main manuscript. (**A**) Calibration proteins: GroEL 14mer (802.6 kDa), thyroglobulin (669 kDa), non-muscle myosin 2b (597 kDa), HSP16.5 24mer (394.8 kDa), β-amylase (224.3 kDa) showing some dissociation at the low concentrations at which we measured, alcohol dehydrogenase (147.4 kDa), BSA (66.4 kDa), streptavidin (52.8 kDa). (**B**) Smooth-muscle myosin. (**C**) Biotin-streptavidin. (**D**) Lipid nanodiscs. (E) Env expressed in the presence and absence of kifunensine. The Kernel bandwidths were 3, 5, 5, 7.5, 10, 10, 12 and 15 kDa with increasing mass for **A**; 9 kDa for **B**; 3 kDa for **C**; 5 kDa for **D**; 10 kDa for **E**.

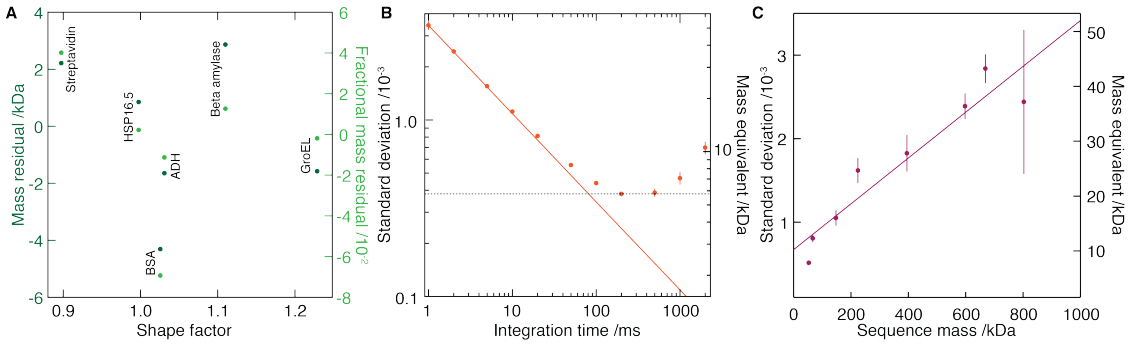


**Fig. S6**

Noise, resolution and shape-dependence characterization. (**A**) Absolute and fractional mass residuals as a function of molecular shape factor(*47*). (**B**) Standard deviation of differential images as a function of integration time, for acquisition at 1000 frames/s. The dashed line indicates the nominal noise floor, and the solid line expectation based on shot noise. (**C**) Standard deviation of contrast histograms obtained for the 8 calibration proteins from Fig. 2A, including a linear fit as a guide to the eye

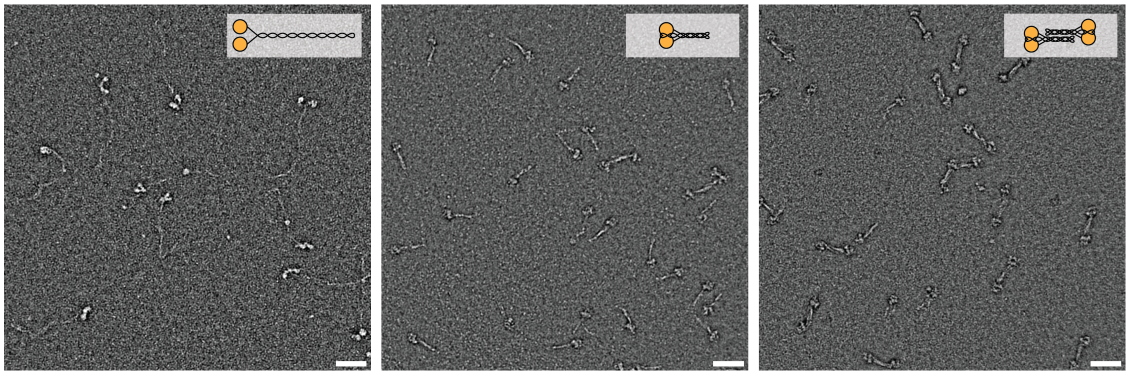

**Fig. S7**

EM images of SMM in the extended (6S, left) and folded (10S, middle) conformation. Cross-linking at 25 mM salt increased the fraction of SMM dimers (right). Scale bar: 50 nm.

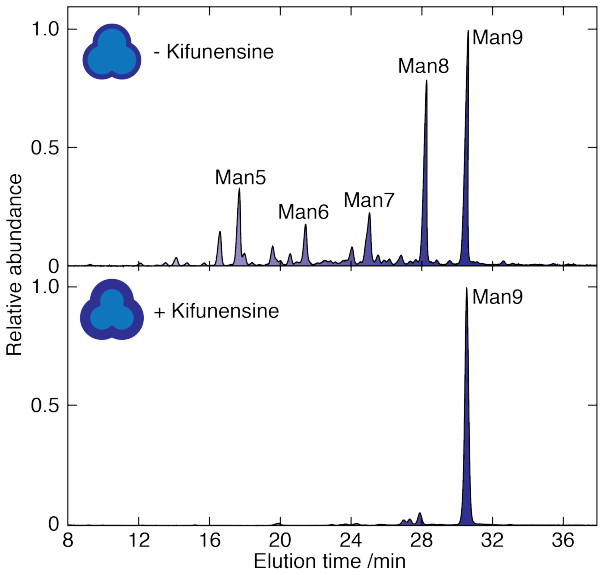


**Fig. S8**

High-performance liquid chromatography of N-glycans released from Env expressed in the absence (top) and presence (bottom) of kifunensine. The corresponding average masses are determined to be 1664 and 1885 Da based on peak height, respectively.

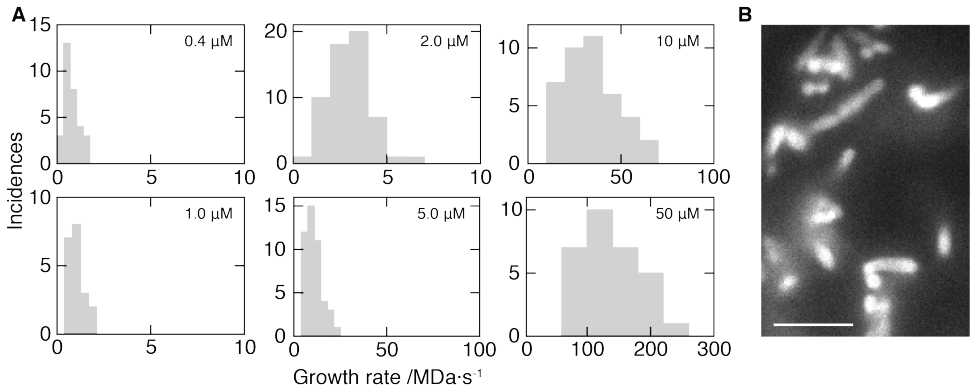


**Fig. S9**

Initial growth rate distribution, and thioflavin-T staining for α-synuclein aggregation. (**A**) Growth rate histograms underpinning Fig. 4B from the main text. Total number of particles analyzed: 31, 20, 58, 46, 40, 30. (**B**) Fluorescence image after thioflavin- T staining of a bilayer aggregation assay at 10 µM after overnight incubation. Scale bar: 5 µm.

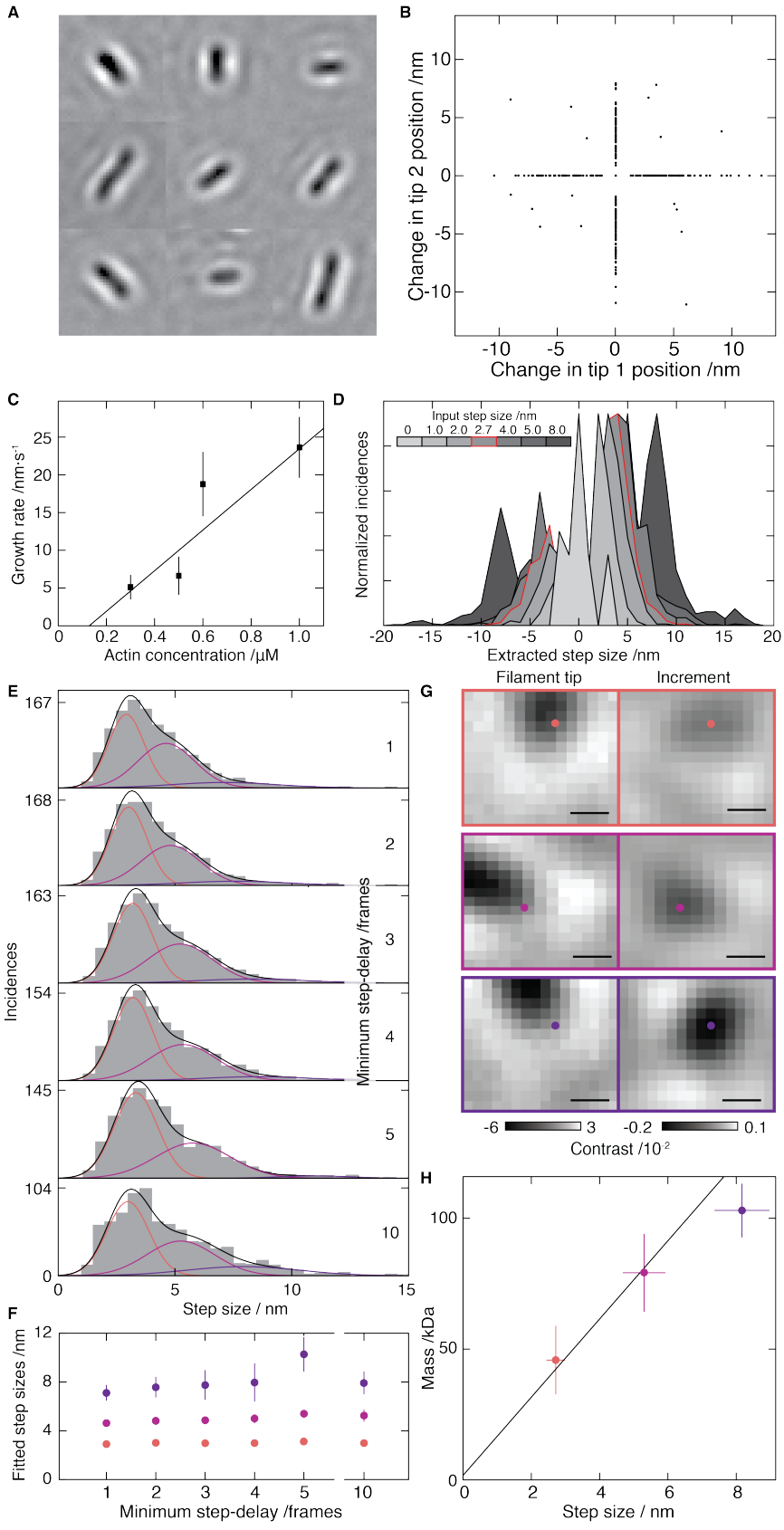
A
B
Change in tip 2 position /nm
Change in tip 1 position /nm
C
Growth rate /nm·s⁻¹
Actin concentration /μM
D
Input step size /nm
0 1.0 2.0 2.7 4.0 5.0 8.0
Normalized incidences
Extracted step size /nm
E
Incidences
Minimum step-delay /frames
Step size / nm
F
Fitted step sizes /nm
Minimum step-delay /frames
G
Filament tip
Increment
Contrast /10⁻²
H
Mass /kDa
Step size / nm

**Fig. S10**

**Addition of actin to individual filaments.** (**A**) Representative 1.7×1.7 μm images of short phalloidin-stabilized actin filaments. (**B**) Scatter plot of detected steps at the two ends of the filament for the filaments from **A**. (**C**) Macroscopic growth rate recorded for 26, 14, 37 and 10 different filaments at increasing actin concentration including a linear fit. (**D**) Step size histograms resulting from applying the step-finding algorithm to simulated step traces with different step sizes. In each case, 16 filaments were simulated with a total number of 1500 steps. The total number of detected steps were 22, 301, 575, 704, 940, 1088 and 1247 for 0-8 nm steps. (**E**) Experimental step size distributions as a function of minimum delay time between steps including fits to a Gaussian mixture model. (**F**) Step sizes determined from **E**. (**G**) Representative images of the growing filament (left) and differential mass image (right) for 2.8, 5.6 and 8.4 nm steps. The points indicate the centre of the differential mass and are overlaid on the image of the filament tip. Scale bar: 200 nm. (**H**) Mass corresponding to 1,2 and 3 subunit additions obtained from images such as those shown in **G**, using 11, 14 and 8 events, respectively. The line indicates a linear fit to 0, 1 and 2 subunit additions to obtain a step size-to-mass conversion.

**Table S1.**

Contributions to R, $V_i$, and $M_i$ for the canonical amino acids.

| Amino acid | $n_{aa}$ /$g$ | $V_i$ /($cm^3$ /mol) | $M_i$ /Da |
|---|---|---|---|
| A | 0.242 | 54.26723 | 89.0932 |
| R | 0.253 | 116.12344 | 174.201 |
| N | 0.229 | 76.79325 | 132.1179 |
| D | 0.227 | 70.52933 | 133.1027 |
| C | 0.238 | 62.33805 | 121.1582 |
| Q | 0.237 | 89.98362 | 146.1445 |
| E | 0.233 | 84.80384 | 147.1293 |
| G | 0.225 | 38.42674 | 75.0666 |
| H | 0.253 | 95.94639 | 155.1546 |
| I | 0.282 | 99.31927 | 131.1729 |
| L | 0.279 | 99.13858 | 131.1729 |
| K | 0.266 | 102.391 | 146.1876 |
| M | 0.263 | 101.00571 | 149.2113 |
| F | 0.287 | 116.54505 | 165.1891 |
| P | 0.245 | 74.14313 | 115.1305 |
| S | 0.22 | 56.73666 | 105.0926 |
| T | 0.236 | 72.276 | 119.1192 |
| W | 0.297 | 139.55291 | 204.2252 |
| Y | 0.272 | 118.71333 | 181.1885 |
| V | 0.27 | 83.77993 | 117.1463 |

**Table S2.**

Composition key (all with MSP1D1 as the scaffold protein). *MSP1D1/DMPC nanodisc taken as reference for size comparison.

| Composition | Lipid | Percentage | Mass/ Da | Average Lipid Mass /Da | Protein:lipid assembly ratio | Relative mass of lipid content |
|---|---|---|---|---|---|---|
| a* | DMPC | 100 | 677.9 | 677.9 | 1:80 | 1 |
| b | DMPC<br>PC14:1<br>Cholesterol | 40<br>50<br>10 | 646.8<br>645.2<br>386.7 | 646.8 | 1:73.5 | 0.877 |
| c | PC14:1<br>Cholesterol | 90<br>10 | 673.9<br>386.7 | 645.2 | 1:67 | 0.797 |

**Table S3.**

Reduction in total mass of nanodisc calculated for a range of measured masses of the MSP1D1 DMPC nanodisc. All values are given in kDa. SEC, DLS and NMR data are from (*48*) and native MS from (*49*).

| MSP1D1 mass | Technique | MSP1D1 lipid mass | Exp. MSP1ΔH5 lipid mass | | | Exp. MSP1ΔH5 nanodisc mass | | |
|---|---|---|---|---|---|---|---|---|
| | | | SEC | DLS | EM | SEC | DLS | EM |
| 141.0 | iSCAMS | 93.9 | 74.6 | 72.9 | 67.4 | 116.6 | 114.9 | 109.4 |
| 124.0 | SEC | 76.9 | 61.1 | 59.7 | 55.2 | 103.1 | 101.7 | 97.2 |
| 126.0 | DLS | 78.9 | 62.7 | 61.2 | 56.6 | 104.7 | 103.2 | 98.6 |
| 149.5 | Native MS | 102.4 | 81.4 | 79.5 | 73.5 | 123.3 | 121.5 | 115.5 |
| 158.0 | NMR | 110.9 | 88.1 | 86.1 | 79.6 | 130.1 | 128.1 | 121.6 |

**Table S4.**

Size comparison for lipid nanodiscs. Reduction in area of lipid bilayer patch in nanodisc with reduction in size of scaffold protein, calculated from reduction in hydrodynamic diameter as measured by SEC, DLS or EM (*48*). D = diameter, $R_{lo}$ = radius of lipid-only content assuming the belt protein contributes 0.5 nm to the radius.

| Technique | MSP1D1 | | MSP1ΔH5 | | Ratio of lipid areas: MSP1ΔH5/MSP1D1 |
|---|---|---|---|---|---|
| | D/nm | $R_{lo}$ /nm | D/nm | $R_{lo}$ /nm | |
| SEC | 10.2 | 4.6 | 9.2 | 4.1 | 0.79 |
| DLS | 9.4 | 4.2 | 8.4 | 3.7 | 0.78 |
| EM | 9.5 | 4.25 | 8.2 | 3.6 | 0.72 |

**Table S5.**

Composition b predictions. All values are given in kDa.

| Mass of MSP1D1 | Lipid mass in MSP1D1 nanodisc | Expected lipid mass | Expected nanodisc mass |
|---|---|---|---|
| 141.0 | 93.9 | 82.3 | 129.4 |
| 124.0 | 76.9 | 67.4 | 114.5 |
| 126.0 | 78.9 | 69.2 | 116.3 |
| 149.5 | 102.4 | 89.8 | 136.9 |
| 158.0 | 110.9 | 97.2 | 144.3 |

**Table S6.**

Composition c predictions. All values are given in kDa.

| Mass of MSP1D1 | Lipid mass in MSP1D1 nanodisc | Expected lipid mass | Expected nanodisc mass |
|---|---|---|---|
| 141.0 | 93.9 | 74.9 | 121.9 |
| 124.0 | 76.9 | 61.3 | 108.4 |
| 126.0 | 78.9 | 62.9 | 110.0 |
| 149.5 | 102.4 | 81.6 | 128.7 |
| 158.0 | 110.9 | 88.4 | 135.5 |

**Table S7.**

Contrast-mass conversions (linear fit parameters to a contrast vs mass calibration plot as shown in Fig 2A) for all data shown in Fig 2. The different datasets were taken at different times, and as a result of the use of partial reflectors of different transmissivity, oxidation of the partial reflector, and minor drifts in alignment, the values for converting between mass and contrast were different over time. The setup was calibrated for each measurement using the procedure outlined for Fig. 2A, and for ease and consistency of display the contrasts shown for each measurement in Figs. 2 and S5 were normalized to the contrast as in Fig. 1.

| Figures | Description | Slope /kDa$^{-1}$ | Intercept |
|---|---|---|---|
| 1, 2B, S5C | BSA; streptavidin-biotin binding, | 6.5651E-05 | 4.2324E-04 |
| 2A, S5A | Representative Calibration | 2.0529E-05 | 3.3099E-04 |
| 2C, S5D | Lipid nanodiscs | 1.6483E-05 | 0.0000E+00 |
| 2D, S5E | Env +/- kifunensine comparison | 1.5410E-05 | 0.0000E+00 |

**Table S8.**

Abbreviations used in Fig. 2. *Exact sequences given on page S4.

| Abbreviation | Meaning | Description |
|---|---|---|
| SEC | size-exclusion chromatography | Experimental techniques used in the literature for mass determination of the MSP1D1/DMPC nanodisc |
| DLS | dynamic light scattering | |
| MS | (native) mass spectrometry | |
| NMR | nuclear magnetic resonance | |
| MSP1D1 | Membrane scaffold protein (MSP) 1 with the first 11 N-terminal amino acids removed, as described in (*50*) | Membrane scaffold proteins (MSPs) used to make the lipid nanodiscs |
| MSP1ΔH5 | MSP1D1 with the 5th α-helix deleted, as described in (*48*) | |
| DMPC | 1,2-dimyristoyl-*sn*-glycero-3-phosphocholine | Lipids used in the lipid nanodiscs |
| PC14:1 | 1,2-dimyristoleoyl-*sn*-glycero-3-phosphocholine | |
| Chol | cholesterol | |
| DSG3 | desmoglein-3 | Biotinylated peptides in Fig 2D* |
| ACTH | adrenocorticotropic hormone | |

**Supplementary references**


31. T. L. McMeekin, M. L. Groves, M. Wilensky, Refractive Indices of Proteins in Relation to Amino Acid Composition and Specific Volume. *Biochem. Biophys. Res. Commun.* **7**, 151–156 (1962).

32. Y. Harpaz, M. Gerstein, C. Chothia, Volume Changes on Protein-Folding. *Structure*. **2**, 641–649 (1994).

33. A. Yildiz *et al.*, Myosin V walks hand-over-hand: Single fluorophore imaging with 1.5-nm localization. *Science*. **300**, 2061–2065 (2003).

34. N. Billington, A. Wang, J. Mao, R. S. Adelstein, J. R. Sellers, Characterization of Three Full-length Human Nonmuscle Myosin II Paralogs. *J. Biol. Chem.* **288**, 33398–33410 (2013).

35. J. R. Sellers, M. D. Pato, R. S. Adelstein, Reversible Phosphorylation of Smooth-Muscle Myosin, Heavy-Meromyosin, and Platelet Myosin. *J. Biol. Chem.* **256**, 3137–3142 (1981).

36. L. Yang *et al.*, An adaptive non-local means filter for denoising live-cell images and improving particle detection. *J. Struct. Biol.* **172**, 233–243 (2010).

37. M. S. Woody, J. H. Lewis, M. J. Greenberg, Y. E. Goldman, E. M. Ostap, MEMLET: An Easy-to-Use Tool for Data Fitting and Model Comparison Using Maximum-Likelihood Estimation. *Biophys. J.* **111**, 273–282 (2016).

38. C. Tzitzilonis, C. Eichmann, I. Maslennikov, S. Choe, R. Riek, Detergent/Nanodisc Screening for High-Resolution NMR Studies of an Integral Membrane Protein Containing a Cytoplasmic Domain. *PLoS ONE*. **8**, e54378 (2013).

39. R. W. Sanders *et al.*, A Next-Generation Cleaved, Soluble HIV-1 Env Trimer, BG505 SOSIP.664 gp140, Expresses Multiple Epitopes for Broadly Neutralizing but Not Non-Neutralizing Antibodies. *Plos Pathogens*. **9**, e1003618 (2013).

40. S. Campioni *et al.*, The Presence of an Air-Water Interface Affects Formation and Elongation of alpha-Synuclein Fibrils. *J. Am. Chem. Soc.* **136**, 2866–2875 (2014).

41. S. S. Lehrer, G. Kerwar, Intrinsic Fluorescence of Actin. *Biochemistry*. **11**, 1211–1217 (1972).

42. F. Ruhnow, D. Zwicker, S. Diez, Tracking Single Particles and Elongated Filaments with Nanometer Precision. *Biophys. J.* **100**, 2820–2828 (2011).

43. Chen, J., & Gupta, A. K. Testing and Locating Variance Changepoints with Application to Stock Prices. *J. Am. Stat. Assoc.*, **92**, 739 (1997).

44. K. C. Holmes, D. Popp, W. Gebhard, W. Kabsch, Atomic Model of the Actin Filament. *Nature*. **347**, 44–49 (1990).

45. T. D. Pollard, M. S. Mooseker, Direct Measurement of Actin Polymerization Rate Constants by Electron-Microscopy of Actin-Filaments Nucleated by Isolated Microvillus Cores. *J. Cell Biol.* **88**, 654–659 (1981).

46. T. D. Pollard, Rate Constants for the Reactions of ATP-Actin and ADP-Actin with the Ends of Actin-Filaments. *J. Cell Biol.* **103**, 2747–2754 (1986).

47. E. G. Marklund, M. T. Degiacomi, C. V. Robinson, A. J. Baldwin, Benesch, Justin L. P., Collision Cross Sections for Structural Proteomics. *Structure*. **23**, 791–799 (2015).

48. F. Hagn, M. Etzkorn, T. Raschle, G. Wagner, Optimized Phospholipid Bilayer Nanodiscs Facilitate High-Resolution Structure Determination of Membrane Proteins. *J. Am. Chem. Soc.* **135**, 1919–1925 (2013).

49. M. T. Marty *et al.*, Native Mass Spectrometry Characterization of Intact Nanodisc Lipoprotein Complexes. *Anal. Chem.* **84**, 8957–8960 (2012).

50. I. G. Denisov, Y. V. Grinkova, A. A. Lazarides, S. G. Sligar, Directed self-assembly of monodisperse phospholipid bilayer nanodiscs with controlled size. *J. Am. Chem. Soc.* **126**, 3477–3487 (2004).